Catalysis Science & Technology

ROYAL SOCIETY OF CHEMISTRY

PAPER

View Article Online
View Journal | View Issue

Cite this: *Catal. Sci. Technol.*, 2026, **16**, 925

Unsupported CoMoS catalysts for isoeugenol hydrodeoxygenation: optimisation of synthesis parameters for catalyst performance

Tyko Viertiö, *[a] Niko Vuorio,[a] Sari Rautiainen, [a] Johanna Kihlman,[a] Alexander Reznichenko,[a] Kristoffer Meinander,[b] Dmitry Yu. Murzin [c] and Juha Lehtonen [a]

Received 13th December 2024,
Accepted 16th December 2025

DOI: 10.1039/d4cy01503g

rsc.li/catalysis

Hydrodeoxygenation of isoeugenol as a model compound for lignocellulosic biomass-derived oils has been studied in this work. A series of unsupported cobalt-doped molybdenum oxide and sulfide catalysts were prepared *via* hydrothermal precipitation to systematically study the effect of catalyst preparation conditions on catalyst properties and catalytic performance. The effects of the preparation temperature, excess sulfur, and pH and their combinations were studied using a design of experiments approach. The catalysts were characterized with ICP-OES, N_2 physisorption, XRD, XPS and SEM-EDS and screened for bio-oil model compound isoeugenol hydrodeoxygenation under relevant process conditions of 300 °C and 30 bar in a batch reactor. Co was observed as a sulfide, while molybdenum exhibited mixtures of the oxide and sulfide, with the former favored under preparation conditions with less sulfur. The catalyst performance testing revealed a higher activity and increased deoxygenation selectivity of the sulfide catalysts compared to those of the oxide catalysts. In addition to the chemical nature, the catalyst activity in the model reaction was increased by the high pore volume and surface area, which were promoted by a low pH at the start of the synthesis. The observed tendencies provide a basis for catalyst tailoring in hydrotreatment processes for biofuel and biochemical production from lignocellulosic biomass.

1 Introduction

Despite the rapid electrification of passenger vehicles, the demand for bio-based liquid fuels is expected to grow in the future as many transportation modes are difficult to electrify. In 2022, the share of biofuels was 4% of the global transportation energy demand[1] of which *ca.* 66% was ethanol.[2] The long-term need is not only to replace fossil fuels with renewable fuels, but also to increase the sustainability of the biofuels by utilizing non-food feed streams such as agricultural and forest residues and wastes.[3] The share of these advanced biofuels in transportation is expected to grow steadily during the coming decades, but an exact prognosis is challenging. Khalili *et al.*[4] reviewed 19 different scenarios for global transportation fuel demand in 2050. Among these, the share of renewable liquid fuels ranged from 0% to 74%, with the average share around 34%. Chiaramonti *et al.*[5] reviewed 18 different papers with 56 scenarios and, based on these, forecast a 13.3% share of advanced biofuels in the transport sector by 2050. IEA[6] predicted, in their Net Zero by 2050 roadmap, that 80% of aviation fuels will be synthetic liquids and advanced biofuels by 2050. According to the ReFuelEU Aviation initiative, 70% of aviation fuel consumption in the EU in 2050 should be covered by sustainable aviation fuel, predicting a demand of 5–10 Mtoe/a of aviation biofuels.[7] Current technologies and feedstocks are not sufficient to meet these future demands; therefore, methods to upgrade even highly challenging bio-based feedstocks are needed.

Thermochemical liquefaction methods of lignocellulosic biomass, for example, fast pyrolysis and hydrothermal liquefaction, produce bio-oils that have a suitable chemical composition to be upgraded to transportation liquid biofuels.[8] These liquefaction processes are feedstock-flexible, enabling the utilization of challenging secondary streams, such as agricultural and municipal solid waste.[9] Fast pyrolysis is particularly suitable for decentralized production, as the product, liquid bio-oil, is easy to transport to a central upgrading facility,[10,11] and this approach has been demonstrated on a commercial scale with multiple operating plants.[10,12] The major challenges in the use of bio-oil are related to the high oxygen content, thermal instability and

[a] *VTT Technical Research Center of Finland Ltd., FI-02044 Espoo, Finland. E-mail: tyko.viertio@vtt.fi*
[b] *Department of Bioproducts and Biosystems, Aalto University, FI-00076 Aalto, Finland*
[c] *Åbo Akademi University, Johan Gadolin Process Chemistry Centre, Henriksgatan 2, Turku/Åbo, 20500, Finland*

impurities originating from the original biomass.[13] Therefore, the use of bio-oil is today limited to heating applications and co-feeding in small quantities to existing catalytic process units such as fluid catalytic cracking (FCC) at oil refineries.[11]

High oxygen content is typically lowered by hydrodeoxygenation (HDO), where high-pressure hydrogen and a catalyst are used at high temperature to remove oxygen as water.[14] Typical HDO catalysts include traditional sulfided hydrotreatment catalysts, noble-metal catalysts,[15,16] reduced base metal catalysts[17–20] and metal carbides, phosphides and nitrides.[21] However, application of these catalysts for actual bio-oil hydrotreatment is typically challenging due to extensive coke formation.[22,23]

The HDO reaction of bio-based oils has been extensively studied during the past decades due to its importance in sustainable fuels and chemicals production.[24] Model compounds are often used for liquid feedstocks derived from lignocellulosic biomass; the most typical model compounds used are phenolic compounds which mimic lignin-based monomers.[24–26] The model compound isoeugenol was selected for this study due to its multiple functional groups, *i.e.* phenolic hydroxyl, methoxy and allyl moieties, representing the typical functionalities of lignin.[27] Moreover, isoeugenol can be fully deoxygenated to cycloalkanes, which are promising components of sustainable aviation fuels (SAF).[28] The HDO of isoeugenol has been previously reported in batch and continuous reactor systems, mainly with reduced metal catalysts supported on various supports ranging from carbon to zeolites.[15,17–19,29–33] Recently, Martinez-Klimov[15] reported isoeugenol hydrodeoxygenation on bimetallic Pt–Re catalysts supported on activated carbon at 250 °C, concluding that the synergistic effect of reduced Pt and Re-oxide species increased the propyl cyclohexane yield and mass balance. Grilc *et al.* studied the HDO of a highly similar compound, eugenol, with sulfided and reduced metal catalysts,[34–36] reporting the formation of dimer compounds with sulfided catalysts.[36] However, we are not aware of isoeugenol HDO studies with sulfided or unsupported catalysts.

Recently, slurry upgrading of bio-oil has been applied to manage catalyst deactivation during bio-oil upgrading. Slurry hydroprocessing, originally developed for challenging, heavy fossil feedstocks with high coke formation propensity and metallic impurity content, enables the removal and addition of catalysts during processing.[37] Slurry hydrotreatment with unsupported molybdenum sulfide catalysts was recently demonstrated with and without fossil cofeeding for bio-oil feed.[38–41]

During the last decade, hydrothermal synthesis of unsupported Mo sulfides for HDO has enabled catalyst tailoring for applications; this has been studied by multiple groups, and the work has been reviewed extensively, for example, by Cao.[42] Liu *et al.*[26] prepared single-layered sulfur-vacancy-rich MoS_2 by Li intercalation and introduced Co doping as isolated atoms in the vacancies using a low-concentration $Co(thiourea)_4^{2+}$ solution. The material showed a 34-fold increase in the reaction rate and 99.2% selectivity in the HDO of p-cresol to toluene at 300 °C by the introduction of the Co-promoter. Wu *et al.*[43] applied a similar approach in the hydrothermal synthesis of MoS_2 and subsequent solvothermal introduction of Co oxides that were reduced to metallic Co by a spontaneous interfacial reaction. Wu *et al.*[44] also introduced a Pt promoter to a MoS_2 catalyst to synthesize active Pt-edge sites on the inactive basal planes to increase the activity of the catalyst. The introduction of Pt also switched the product distribution towards hydrogenated product methylcyclohexane with a selectivity of >90%; typically, toluene selectivities of >90% are reported for Co-doped catalysts.[25,26,43–47]

Recently, Zhou *et al.*[48] demonstrated the effect of oxygen defect preparation on MoS_2 by oxygen etching at temperatures between 300 and 600 °C. In their procedure, the catalyst is first precipitated and afterwards exposed to O_2 at high temperature to create catalytically active surface defects. Zhou *et al.* highlight the role of different defects on the surface: they observed the highest reaction rate of m-cresol HDO on catalysts oxygen-etched at 350 °C with no sulfur Mo^{4+-3+} sites but a high number of Mo^{5+} oxygen defects. However, not only were the Mo^{5+} defects found to define the catalyst's activity, but the role of MoS_2 was also crucial for the dissociation of H_2 on the catalyst surface of the most active catalyst. Conversion of m-cresol increased from 6% to 30% at 300 °C under atmospheric pressure by oxygen etching of the catalyst at 350 °C.[48] Previously, an etching process utilizing H_2O_2 was also presented by Zhang *et al.*,[49] and they showed that increasing the surface acidity increased the conversion of *p*-cresol.

Cao *et al.*[25] investigated the effect of the active cobalt phase in Co-promoted MoS_2 catalyst. They synthesised the MoS_2 catalyst hydrothermally, introduced Co as a hydrothermal precipitation to form a CoS_2/MoS_2 catalyst, and impregnated Co on MoS_2 to form a Co–Mo–S catalyst. Both Co addition methods, hydrothermal precipitation and impregnation, significantly increased the conversion of the model compound *p*-cresol from 12.6% to 58.9% and 88.5%, respectively; however, remarkably improved conversion and selectivity to toluene was achieved with the impregnated Co–Mo–S catalyst. This result was attributed to better synergistic effect between the Co promotor and MoS_2, observed as decreased reduction temperature of sulfide vacancies in H_2-TPR.

In their previous work, Cao *et al.*[45,47] investigated the effect of the preparation parameters of the hydrothermal synthesis, essentially pH and sulfur precursor content, on surface defects in the preparation of Co-promoted MoS_2. An increase in the amount of thiourea precursor and a low pH of 0.9 increased the number of defect sites in the prepared MoS_2, enabling the incorporation of more dispersed Co promoters to form active Co–Mo–S sites on the MoS_2 basal planes.

Cheah *et al.*[50] annealed their hydrothermally precipitated MoS_2 catalyst at 400 °C in an inert gas flow and reported an

increased number of defect sites, based on HRTEM images. The annealing increased the yield of fully deoxygenated products from the model compound, propyl guaiacol, from 49.6% to 80.4%.

To summarize these literature observations, the optimal Co-doped MoS_2 catalyst contains a high number of defects for optimal formation of active Co–Mo–S sites, with Co present at the atomic scale. The catalyst is a mixture of sulfide and oxide phases, as the hydrogen dissociation capability of MoS_2 and Co phases supplies hydrogen for the Mo^{5+} sites responsible for HDO.

In this paper, we studied the design space for the robust one-step hydrothermal synthesis of Co-doped MoS_2 catalysts by applying the following catalyst preparation parameters: starting pH of the synthesis, synthesis temperature and sulfur loading in the synthesis. The prepared catalysts were extensively characterized and evaluated in the HDO of the bio-oil model compound isoeugenol, as presented and summarized in the results (section 3). The effect of the prepared catalysts' material properties on the catalytic behaviour and the preparation conditions on the catalysts' material properties are covered in the discussion (section 4). To the best of our understanding, this is the first report of an extensive design matrix and screening of catalyst preparation conditions, as well as using isoeugenol as a model compound, with this type of catalyst. The results were utilised to scale up the catalyst preparation for application in pilot-scale slurry hydrotreatment test runs of fast-pyrolysis bio-oil,[51] which are reported separately.

2 Experimental

2.1 Catalyst preparation

Unsupported CoMoS catalysts were prepared by a hydrothermal synthesis method inspired by the literature reports.[50,52] To study the design space of the catalyst preparation conditions, a full factorial experimental design of the preparation parameters—temperature, molar sulfur excess S/(Mo × 2) and pH—was implemented for identifying their effects on catalyst composition, catalyst characteristics and catalyst performance in HDO. The parameters used are presented in Table 1, and the experimental design is illustrated in Fig. 1.

Table 1 Catalyst synthesis conditions

Catalyst	Synthesis temperature	Molar S/(2 × Mo)	Synthesis pH
Cat-000	200	1	0
Cat-001	200	1	0.8
Cat-010	200	2	0
Cat-011	200	2	0.8
Cat-100	240	1	0
Cat-101	240	1	0.8
Cat-110	240	2	0
Cat-111	240	2	0.8
Center point (three repetitions CatCen 1, 2, 3)	220	1.5	0.4

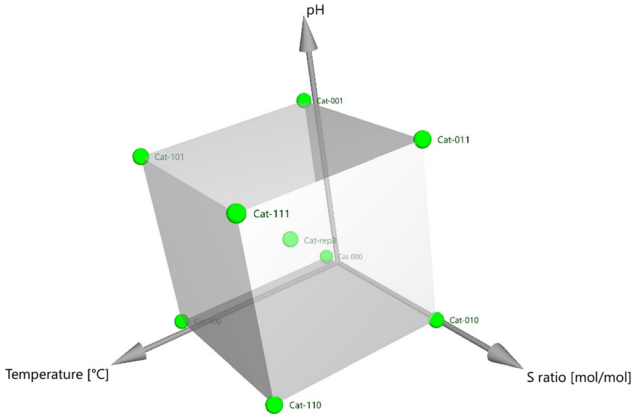

Fig. 1 Design space for the catalyst synthesis.

For the catalyst synthesis, 0.64 g ammonium heptamolybdate ($(NH_4)_6Mo_7O_{24}{\cdot}4H_2O$) (VWR), 0.53 g cobalt nitrate hexahydrate ($Co(NO_3)_2{\cdot}6H_2O$) (Acros Organics) and 0.55 g, 0.83 g or 1.10 g thiourea (CH_4N_2S) (VWR) were weighed and dissolved in 20 mL of ion-exchanged water. The pH of the mixture was measured and adjusted with 37% HCl (VWR) to 0.8, 0.4 or 0, as specified in Table 1. The color of the mixture switched from red to black during pH adjustment. The precursor solution was transferred to a 40 mL steel autoclave with a PTFE cup and PTFE-coated thermowell. The autoclave was pressure-tested and heated to temperatures of 200 °C, 220 °C or 240 °C, as specified in Table 1, with a heating plate and heating jacket, while stirring with a magnetic stirrer bar. Upon reaching the target synthesis time of 20 hours, the heating was turned off, and the autoclave was allowed to cool to room temperature. The catalyst was recovered from the solution by filtration, and the filtrate was washed three times with ethanol (Aa grade, Altia, Finland). The catalyst was dried under vacuum at 60 °C and stored in a glove box under a nitrogen atmosphere, with short exposures to air during sample preparation for further characterization and reaction tests. Due to the small size of the preparation vessel, each synthesis was repeated twice, and the batches were mixed for characterization and reaction experiments. The catalysts were named as shown in Table 1: Cat-TSpH, where T is either 0 or 1, indicating that the synthesis temperature was 200 °C or 240 °C, respectively. Similarly, S and pH indicate either low or high sulfur amount as well as low and high pH, with each being assigned as 0 or 1, respectively.

2.2 Catalyst characterization

Catalysts were characterized with N_2 physisorption, scanning electron microscopy, ICP-OES, XPS and XRD.

2.2.1. N_2 physisorption. N_2 adsorption–desorption was performed with a Micromeritics 3Flex 3500 instrument in liquid nitrogen. Before the analysis, the samples were degassed in a Micromeritics VacPrep instrument for a minimum of 18 hours at 120 °C.

2.2.2. SEM-EDS. The morphology and structure of the catalysts were studied using a Carl Zeiss Merlin field-emission scanning electron microscope (FESEM) with an acceleration voltage of 2 kV.

2.2.3. ICP-OES. The concentrations of the catalyst elements Co, Mo and S, and potential contamination caused by the synthesis reactor steel Al, Cr, Cu, Fe, Mn, Ni and Zn in 11 catalyst samples were measured with ICP-OES (5100 SVDV, Agilent Technologies, Santa Clara, CA, USA). The solids were first treated in a microwave (Ethos Up, Milestone, Sorisole, Italy) with an acid-assisted digestion method by weighing 0.1 g of sample into the microwave tubes. Then, 9 mL HNO_3 (Empura 65%, Merck) and 1 mL H_2O_2 (Suprapur 30%, Merck) were added to the tubes. Three microwave blank samples were included in the sample series. The tubes were closed and placed in a microwave digestion system. The following digestion method was run: 1) temperature was increased to 210 °C in 20 minutes, 2) temperature was held at 210 °C for 15 minutes. After the samples had cooled, they were diluted to 50 mL with ultrapure type 1 water (Synergy® UV Water Purification System, Merck Millipore). Prior to the analysis, the solutions were filtered with syringe filters (0.45 μm). The elements were analysed with ICP-OES equipment from 1/100 and undiluted samples. Dilutions were made with 1% nitric acid solution (Empura 65%, Merck). Multi-elemental standard solutions provided by Inorganic Ventures and Merck were used as calibration standards and control samples in the ICP-OES measurements.

2.2.4. XPS. The measurements were performed with a Kratos AXIS Ultra DLD X-ray photoelectron spectrometer using a monochromated $Al_{K\alpha}$ X-ray source (1486.7 eV) run at 100 W. A pass energy of 80 eV and a step size of 1.0 eV were used for the survey spectra, while a pass energy of 20 eV and a step size of 0.1 eV were used to record the high-resolution spectra of the Mo 3d, S 2p, and Co 2p regions. Photoelectrons were collected at a 90° take-off angle under ultra-high vacuum conditions, with a base pressure typically below 1×10^{-9} Torr. All spectra were charge-corrected relative to the position of C–C bonding of carbon at 284.8 eV.

2.2.5. XRD. X-ray diffractograms were measured with a PANalytical X'Pert Pro MPD in Bragg–Brentano geometry using Cu Kα radiation (λ = 1.5419 Å), programmable divergence and anti-scatter slits, and PIXcel detector in 1D mode. The measurement was in the 2θ range of 10–70° in 0.039° steps.

2.3 Catalyst screening

The prepared catalysts were tested for hydrodeoxygenation of the bio-oil model compound isoeugenol in a batch reactor at 30 bar and 300 °C. In a test run, 100 mL of solvent dodecane (Merck) and 3 g of isoeugenol (Merck) were loaded into a 200 mL Buchi Novoclave autoclave with C276 wetted parts (maximum pressure and temperature 500 bar and 400 °C, respectively). 0.10 g of catalyst was added, giving a catalyst-to-reactant ratio of 1 : 30. 0.23 g of dimethyl disulfide (DMDS, Merck) was added to maintain the sulfidation state of the catalyst during the test run.

In a typical test run, the autoclave was pressure-tested with nitrogen (Woikoski, Finland) with stirring on, and flushed 5 times with hydrogen (Woikoski, Finland). The stirring was stopped, and the reactor was pressurized to 30 bar with hydrogen, and the temperature and pressure were recorded. The autoclave was heated to 300 °C in *ca.* 50 min. The test run time and stirring were started, and the first sample was taken when the internal temperature of the reactor reached 300 °C. According to the ideal gas law, the initial hydrogen partial pressure at 300 °C was estimated to be 59 bar. The samples were taken *via* a dip tube and a sampler at 0, 5 and 30 min and, thereafter, every 30 min until the end of the experiment at 180 min. Two samples were extracted at a time: the 1st to flush the sampling line and the 2nd for the analysis. Taking a sample caused a slight drop in the pressure in the reactor, which was not compensated for. The samples were analysed by gas chromatography using the procedure described below. After reaching the final reaction time and taking the last sample, the reactor was cooled to room temperature. When cooled, the temperature and pressure were recorded, and the gas sample was introduced to a sampling bag from the headspace of the reactor.

2.4 Product analysis

The gas samples from the gas bags were analysed for non-condensable gases and light hydrocarbons using an Agilent 490 micro-GC equipped with four columns (10 m Molsieve-5A, 10 m PoraPLOT-U, 10 m Al_2O_3-KCl and 8 m CP-Sil 5 CB) and four TCDs. The molar amounts of the gas-phase products were calculated using the ideal gas law.

The liquid samples for GC analysis were prepared by mixing (9 : 1 ratio) the sample extracted from the reactor and an internal standard solution of 1.0 mg *n*-hexane (VWR) in 10.0 mL *n*-dodecane. The prepared samples were analysed with a gas chromatograph equipped with an Agilent ULTRA 119091A-115 capillary column (50 m × 320 μm × 0.52 μm) and a flame-ionization detector (GC-FID). The products were identified with an Agilent 6890 series GC system, equipped with an Agilent 5973 mass-selective detector and a DB-5 MS capillary column (30 m × 0.25 mm, film thickness 0.25 μm). The MS identifications were based on the commercial Wiley database.

The response factors for GC-FID were calibrated for isoeugenol (Merck), 4-propyl catechol (abcr Gute Chemie), dihydroeugenol (Sigma-Aldrich), 4-propyl phenol (TCI), guaiacol (Sigma-Aldrich), propyl benzene (TCI) and propyl cyclohexane (TCI Europe), which represent the majority of compounds detected by GC. The response factors for other products detected with GC-MS were estimated based on the response factors defined for the model compounds.

To avoid the effects of measurement deviation due to catalyst load (100 mg ± 10 mg), the reaction time was normalized with the catalyst loading, as presented below.

$$t = \frac{t_r}{m_{cat}} \quad (1)$$

where t is the relative time per catalyst mass, t_r is the actual reaction time in minutes, and m_{cat} is the catalyst mass.

The mass balance at reaction time t is calculated as the amount of GC-detected cyclic compounds.

$$LPMB_t = \frac{n_{all_t}}{n_{IE_0}} \quad (2)$$

where $LPMB_t$ is the liquid-phase mass balance at time t, n_{all_t} is the amount of detected cyclic compounds in moles at time t, and n_{IE_0} is the initial amount of isoeugenol at the start of the test run.

Since the hydrogenation of the isoeugenol double bond is a fast reaction and 100% conversion of isoeugenol was reached in each of the test runs, conversion of the reactants at time t is defined as conversion of both isoeugenol (IE) and dihydroeugenol (DHE).

$$X_t = 1 - \frac{n_{IE_t} + n_{DHE_t}}{n_{IE_0}} \quad (3)$$

where n_{IE_t} and n_{DHE_t} are the amounts of isoeugenol and dihydroeugenol detected at time t, respectively.

The yield of compound a at reaction time t is calculated from the measured concentration, as presented in eqn (4), where n_{a_t} is the amount of compound a at reaction time t.

$$Y_{a_t} = \frac{n_{a_t}}{n_{IE_0}} \quad (4)$$

Due to the low mass balance and oligomer formation discussed below, a group of GC undetected compounds was introduced, as calculated from the mass balance.

$$Y_{undetected_t} = 1 - \frac{n_{all_t}}{n_{IE_0}} \quad (5)$$

The selectivity of compound a at reaction time t is defined as presented in eqn (6). Selectivity is calculated based on yield to enable the calculation of selectivity also for GC undetected compounds presented in eqn (5).

$$S_{a_t} = \frac{Y_{a_t}}{X_t} \quad (6)$$

3 Results

As described in section 2.1, a set of hydrothermally precipitated Co-promoted Mo sulfide catalysts was prepared to study the effects of preparation temperature, pH and sulfur availability on catalyst characteristics and performance. In this section, the results of catalyst preparation, characterization and screening experiments are presented. First, the catalyst preparation results are presented for each method, and then the catalysts are grouped based on the observed properties.

3.1 Characterization results

3.1.1. Elemental analysis. The results of the elemental analysis of fresh catalyst samples by ICP-OES are presented in Table 2. In addition to elements Co, Mo and S, introduced during the catalyst preparation, the samples were studied for steel and catalyst preparation reactant-based contaminants Al, Cr, Cu, Fe, Mn, Ni and Zn. No significant presence of these impurities was detected in the catalysts, as presented in Table A in the Supplemental Information. Unfortunately, measuring oxygen, nitrogen, carbon, and chlorine was not possible with the used method. However, the mass balance of the elemental analysis is expected to be completed with oxygen as oxide materials, as supported by XPS and XRD results (see below and the SI).

3.1.2. Surface morphology. The measured BET surface areas and calculated pore volumes for the samples are presented in Table 3. All isotherms represented the IUPAC classification IV(a), referring to mesoporous materials with pores wider than 4 nm,[53] and hysteresis type H3, referring to non-rigid aggregates of plate-like particles. The SEM images of selected catalysts are presented in Fig. 2; further images are included in the SI (Fig. A).

3.1.3. XRD. XRD was used to determine the crystalline phases present in each catalyst sample (Fig. 3).

The most abundantly detected phase in the XRD analysis of the fresh catalyst samples is CoS_2, identified by the peaks at 2θ = 32°, 35°, 39°, 46° and 56 °, assigned with red arrows in Fig. 3. Crystalline CoS_2 was detected in all the samples except for Cat-000 and Cat-010, which were overall less crystalline materials without significant peaks and contained low amounts of cobalt, based on ICP analysis. Co can also be detected as CoO and Co_3O_4 as traces in some samples.

Mo was detected mainly as MoO_2 and MoS_2 phases. The MoO_2 phase was identified in catalysts Cat-001, Cat-101 and Cat-100, as well as in Cat-000 as sharp peaks at 2θ = 26°, as well as wider peaks at 2θ = 36–37°, 54–55°, 60–61° and 67°, marked with blue arrows in Fig. 3. MoO_3 was identified as minor peaks in catalysts Cat-001 at 2θ = 20°, 27° and 43°, highlighted with black arrows in Fig. 3. MoS_2 was detected as a broad peak at 2θ = 14°, 33° and 58° in some of the samples, especially Cat-111 and Cat-110, as indicated with yellow

Table 2 Elemental content of the catalyst determined by ICP-OES

	Wt%			
	Identified compounds total	Co	Mo	S
Cat-001	86%	20%	36%	29%
Cat-101	74%	14%	38%	21%
Cat-011	95%	14%	39%	43%
Cat-111	99%	13%	41%	45%
Cat-000	78%	1%	52%	24%
Cat-100	77%	10%	46%	20%
Cat-010	93%	13%	39%	41%
Cat-110	94%	3%	41%	49%
CatCen1	93%	16%	36%	40%
CatCen2	89%	15%	36%	38%
CatCen3	92%	16%	34%	42%

Table 3 Physisorption results

Catalyst	BET ($m^2\ g^{-1}$)	Pore volume ($cm^3\ g^{-1}$)
Cat-001	41	0.10
Cat-101	46	0.16
Cat-011	29	0.06
Cat-111	21	0.08
Cat-000	236	0.34
Cat-100	43	0.16
Cat-010	47	0.20
Cat-110	83	0.26
CatCen1	148	0.31
CatCen2	103	0.20
CatCen3	126	0.27

arrows in Fig. 3. To conclude, in Cat-001, Mo was detected as MoO_2 and MoO_3, in Cat-101, Cat-000, Cat-100 as MoO_2, in Cat-011 as MoO_2 and MoS_2, and in Cat-111, Cat-110, and center points as MoS_2.

3.1.4. XPS. The catalyst samples were analyzed by XPS to identify and quantify the different species on the catalyst surface. The abundance of different elements on the catalyst surface, calculated from the XPS spectra of the fresh catalyst samples, is presented in Table B in the SI, and the relative abundance of particular species of Co, Mo, S and O is presented in Table C. Typical high-resolution spectra, including fitted components, for the Mo 3d, S 2p, Co 2p, and O 1s regions are shown in Fig. B in the SI.

The high-resolution spectrum of Mo 3d was fitted with typical doublet-split peaks ($3d_{5/2}$ and $3d_{3/2}$), with fixed energy separation, area ratio, and full width at half maximum, for the expected components of Mo^{4+}, with a $3d_{5/2}$ energy at approximately 228.8 eV, as well as higher oxidation state components of Mo^{5+} at 230.8 eV and Mo^{6+} at 232.5 eV. Additionally, a peak at 227.9 eV, possibly associated with Mo^{2+}, and a peak between Mo^{4+} and Mo^{5+} at 229.7 eV, possibly corresponding to a mixed state of $CoMoS_2$ or a partially oxidized sulfide, were also included.

The sulfur S 2p region typically shows a simple convolution of the S $2p_{3/2}$ and S $2p_{1/2}$ doublet, with a $2p_{3/2}$ energy at approximately 161.8 eV, corresponding to S^{2-}, for molybdenum sulfide samples. This was also the most abundant component in all the samples. Up to five different doublets were, however, needed in the S 2p spectra to achieve a good fit. A small shoulder at approximately 162.4 eV, corresponding to S_2^{2-}, was occasionally detected, while the final three components were rare. The highest energy component, found in sample Cat-000 at 166.0 eV, is typical for sulfites, while the others, located at 161.0 eV and 163.3 eV, are possibly the result of mixed sulfides and partially oxidized sulfides, respectively.

The $2p_{3/2}$ peaks were used for fitting of components to the Co 2p spectra, with two components at 778.6 eV and 780.4 eV, together with two satellites, typically associated with Co 2p peaks. The lower energy component can be associated with CoS_2, while the higher energy component can be associated with CoO.

The oxygen O 1s spectra could be fitted with three peaks, at energies of approximately 530.1 eV, 531.6 eV, and 533.2 eV. The lowest energy component can be associated with oxides of both Mo and Co, while the middle-energy component would be typical for surface hydroxylation of these species. High concentrations of hydroxyls usually point toward a high degree of surface oxidation. The highest energy component, which is also the one with the lowest intensity, might be the result of a mixed oxide or possibly organic surface contamination. Compared to the bulk elemental composition

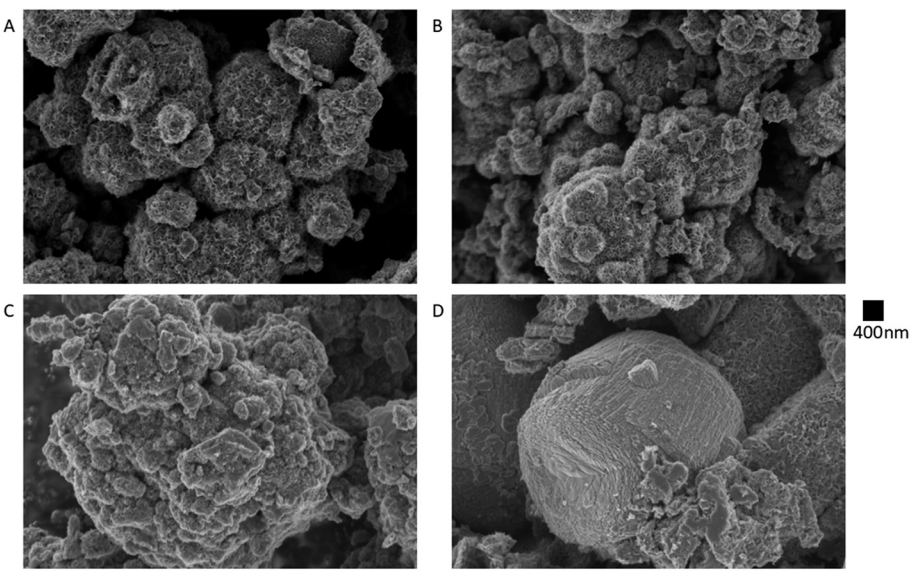

Fig. 2 SEM figures of the selected catalysts. A: Catalyst CatCen3, with sulfide-like nanosheet morphology; B: catalyst Cat-110, with sulfide-like morphology; C: catalyst Cat-000, with non-sulfidic morphology; D: catalyst Cat-101, with non-sulfidic morphology. Acceleration voltage 2 kV and magnification 15 000×.

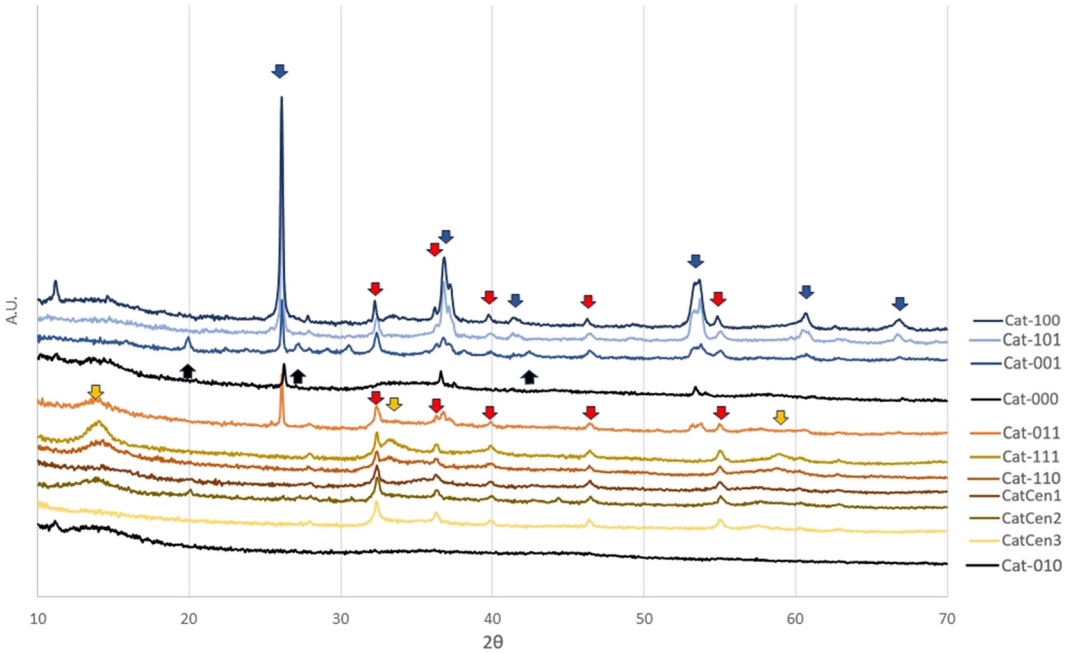

Fig. 3 XRD analysis of the catalysts. The arrows indicate peaks for MoO_2 (blue), CoS_2 (red), MoO_3 (black), and MoS_2 (yellow).

measured by ICP (Table 2), the XPS analysis shows a higher abundance of oxygen species on the surface, which indicates surface oxidation of the samples due to handling in air.

3.2 Catalyst properties

Based on the results of the catalyst characterization, especially by XRD and ICP, the catalysts can be divided into three groups of materials, *i.e.* oxide, sulfide and amorphous materials. Sulfide catalysts Cat-111 and Cat-110 and CatCen materials were characterized by a dominating MoS_2 phase, while for the oxide catalysts Cat-001, Cat-101 and Cat-100, either MoO_2 or MoO_3 was the dominant oxide phase. Catalyst Cat-011 shows both sulfidic and oxidic nature according to XRD; however, based on the reaction performance, it is classified as a sulfide. In both sulfide and oxide catalysts, cobalt was detected as the CoS_2 phase by XRD. Amorphous catalysts Cat-010 and Cat-000 were outliers in the XRD, with only weak peaks of Mo phases, no CoS_2 and low Co in the ICP analysis. In this subsection, the characterization results are summarized by using these groupings to highlight differences between the catalyst groups. The catalytic behaviour is discussed and compared based on the presented grouping of catalysts (*vide infra*).

3.2.1. Oxide materials Cat-001, Cat-101 and Cat-100. The elemental composition of the bulk catalysts presented in Table 2 shows that the Co content of these catalysts is 10–20 wt%, while the Mo content is 36–46 wt% and S is 20–29 wt%. The sulfur content was low compared to the average of the other catalysts, which were measured to be 40%. The sum of identified elements (73–86 wt%) indicated high amounts of unidentified elements, probably containing mostly oxygen. The identified elements in the XPS supported this assumption, as the calculated amounts of Co, Mo, S and O on the surface of the oxide catalysts were 2–5 wt% Co, 56–58 wt% Mo, 25–32 wt% S and 8–14 wt% O.

In the XRD patterns presented in Fig. 3, crystalline MoO_2 was detected in all samples, and MoO_3 was also detected in sample Cat-001. Cobalt was present as CoS_2. The same observations were made based on the XPS data, as a high amount of surface oxygen species was detected, assigned to oxide and hydroxyl groups, indicating a high degree of surface oxidation (see Table C in the SI).

The XPS results indicated Mo^{6+} species of MoO_3 and high surface oxygen are abundant, especially in Cat-001. In Cat-101, the surface contained Mo^{4+} and high amounts of oxide and sulfide species, while Cat-100 was high in Mo, S and O species, indicating the presence of mixed sulfides and oxides. The BET surface areas of the oxide catalysts were nearly identical, with surface areas being 41, 43 and 46 $m^2\ g^{-1}$ for Cat-001, Cat-100 and Cat-101 catalysts, respectively. Based on SEM analysis, the morphology of the oxide catalysts is clearly different from the sulfide catalysts, showing more variation and lacking the typical sulfide nanosheets[54] (Fig. A, SI).

3.2.2. Sulfide catalysts Cat-011, Cat-111, Cat-110 and center point catalysts. The center point catalysts, classified as sulfide catalysts, are very similar to each other, with only minor variations. A lower mass balance closure for CatCen2 was explained by a higher fraction of the oxide compared to the sulfide, which is supported by the XPS data presented in Table B in the SI.

The XRD results in Fig. 3 indicate that CatCen1, CatCen2 and CatCen3 catalysts all contain a crystalline CoS_2 phase as the only clearly identifiable phase. MoS_2 was also detected as

broad peaks. CatCen1 and CatCen2 also show traces of crystalline MoS_2 and $CoMoS_2$ phases, whereas no other crystalline phases are detected in CatCen3.

The previously mentioned minor deviations in the ICP and XRD analyses are supported by the XPS analysis presented in Tables B and C in the SI. Cobalt is detected in similar amounts in all samples, whereas more oxygen is detected on the surface of the CatCen2 catalyst, compared to CatCen1 and CatCen3, as expected from a lower ICP mass balance. Based on XPS, oxygen is detected mainly as the oxide and as surface OH, indicating incomplete sulfidation during catalyst preparation, and surface oxidation.

Sulfide catalysts Cat-011, Cat-111 and Cat-110 are characterized to a large extent by a similar elemental composition, surface morphology and crystal structure to those of the CatCen catalysts.

BET surface area is the first key difference between these sulfide materials. As can be seen in Table 3, surface areas of between 103 $m^2\ g^{-1}$ and 148 $m^2\ g^{-1}$ are measured for the CatCen catalysts, which differ significantly compared to those of the other sulfide catalysts, with surface areas from 21 to 83 $m^2\ g^{-1}$, as well as to the oxide materials.

The SEM experiments also confirmed the difference in materials, as a typical MoS_2 surface with nanosheet[54] morphology can be detected, especially in sulfide catalysts CatCen3 and Cat-110 catalysts, compared to Cat-000 and Cat-101 catalysts, as shown in Fig. 2.

3.2.3. Highly amorphous catalysts Cat-000, Cat-010. Catalysts Cat-000 and Cat-010 were synthesized at high temperature and low pH, and are low-crystalline in nature, based on XRD characterization. Interestingly, these catalysts also form the most significant outliers when comparing the preparation conditions and characterization data to catalytic performance.

Catalyst Cat-000, prepared at a low temperature of 200 °C, low pH of 0, and a low S : Mo molar ratio (1 : 1), stood out in all of the measured parameters. The amount of cobalt is the lowest of all the synthesized catalysts, with 0.6 wt% and 0.5 wt% detected by ICP and XPS, respectively, compared to the average for the synthesised catalysts of 3.0 wt% and 10.8 wt%, respectively. A significant amount of oxygen was also detected by XPS, 16.7 wt% compared to the average of 7.8 wt%, which is in good agreement with the low mass balance closure of ICP measurements of 23.8 wt% compared to the average of 13.8 wt%. The catalyst BET surface area was very high (236 $m^2\ g^{-1}$), being over three-fold higher than the average of 68 $m^2\ g^{-1}$. XRD demonstrated that this particular catalyst is highly amorphous, with molybdenum oxide being the only detected crystalline phase. Furthermore, XPS displayed a high amount of the oxide instead of the typically observed sulfide. However, the catalyst was not characterized after the reaction; thus, the five-fold excess of sulfur in the test run could affect the oxygen–sulfur ratio of the catalyst after the test run.

On the other hand, catalyst Cat-010 was prepared by applying similar conditions, but with a high sulfur loading. The catalyst has the highest S content based on the ICP and XPS analysis. The amount of oxygen in the catalyst is low, mainly present as hydroxyls, as can be seen in Table C in the SI. Based on low Co content in ICP of both materials, Cat-010 and Cat-000, it was concluded that the low pH in combination with low T prevents formation of Co sulfide during catalyst synthesis and therefore hinders Co recovery to the catalyst material.

The low crystallinity of Cat-010 proposed based on the XRD data is also supported by XPS, indicating that the detected Mo and S support the formation of mixed sulfide phases. Mo^{2+}, and especially Mo^{4-5+}, phases are detected in high quantities compared to other materials. Sulfur was detected as a typical sulfide phase, but a significant portion of sulfur was assigned to the peak at 163.3 eV, representing partially oxidized sulfides. The surface area of this catalyst was 47 $m^2\ g^{-1}$.

3.3 Catalyst screening experiments

The prepared catalysts were tested in the hydrodeoxygenation of the bio-oil model compound isoeugenol in a batch reactor. Isoeugenol (3 g) and 0.10 g catalyst were mixed with 100 mL of dodecane and heated at 300 °C for 3 h with 30 bar H_2 loading. The products were analyzed by GC. Due to the relatively low mass-balance, discussed below, the reaction performance is described using conversion and yield as key parameters, as described by the equations presented in section 2.4.

3.3.1. Mass-balance. The detected mass balances in the experiments were relatively low (60–90% of the original feed; see Fig. C in the SI). The variance in the mass balance was assigned to the formation of heavier molecular weight compounds not detectable by GC and condensation of heavy products on the catalyst surface. A similar trend was noted in all test runs, as the mass balance decreased and stabilized during the first half of the reaction time of 180 min, and then increased. Further increasing trend of mass balance was confirmed in an extended test run of 240 min with catalyst CatCen3, as shown in Fig. 6. Plotting the mass balance as a function of calculated conversion showed increasing mass balance after conversion of 80%, implying that the formation of GC-undetectable compounds is reversible. These undetected compounds could at least partially be considered as intermediate products, as seen in Fig. C and D in the SI. Interestingly, the catalyst type affected the mass balance and amount of undetected compounds significantly, as will be discussed in section 5.2.

Similar observations have been presented by other researchers studying isoeugenol hydrodeoxygenation.[15,30,31] Several investigators have proposed oligomerization mechanisms for guaiacol and alkyl- and allyl-substituted guaiacol compounds,[36,55,56] aligning with the results presented here with lower mass-balance.

3.3.2. Conversion. The evolution of the conversion of isoeugenol and dihydroeugenol for different catalysts is presented in Fig. 4, while the conversions in the batch tests after a reaction time of 1500 min g_{cat}^{-1} are given in Fig. 5. Practically all the isoeugenol reacted rapidly to

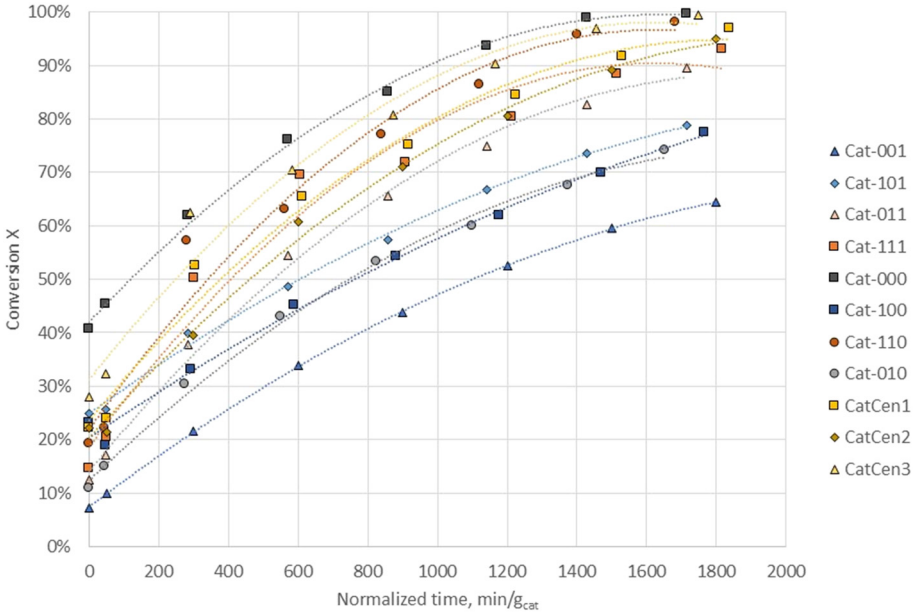

Fig. 4 Conversion as a function of normalized reaction time.

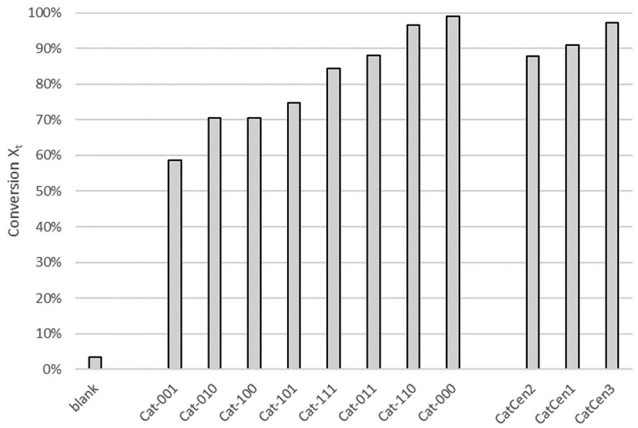

Fig. 5 Conversion after a reaction time of 1500 min g_{cat}^{-1}.

dihydroeugenol and disappeared in all the test runs after 60 min reaction time, except in the blank run. Significant differences were detected between the catalysts, starting from the initial conversions ranging from 7% to 40% and final conversions from 64% to 100%. As the test runs were performed similarly, the differences in the initial concentrations are assigned to reactions taking place during the heating period of the reactor, which were carried out without stirring but in the presence of the catalyst, reactant, and hydrogen. Therefore, the observed initial conversion was interpreted to represent the catalytic activity. However, further comparison of the catalysts is based on calculated reaction rate and selectivity, as described and discussed below.

Based on the observed decrease in the amounts of reactants isoeugenol and dihydroeugenol, 1st order reaction kinetics with respect to isoeugenol and dihydroeugenol were observed as the best fit of linearization among the studied 0th, 1st and 2nd orders, and reaction rate constants were calculated from the observed decrease of reactants for reaction time 0-120 min. Pseudo-0th-order was assumed for hydrogen, as the excess of hydrogen is significant, the pressure of the reactor, and the amount of hydrogen detected in the gas phase samples were in the same range in all experiments. The calculated constants are presented in Fig. H in the SI. The linearization and fitting of the rate constants are presented in the SI.

3.3.3. Product distribution and selectivity. To monitor the development of product yields, selectivity and mass balance loss reversibility, a prolonged test run of 240 min was performed with catalyst CatCen3. The selection of the catalyst for the test run was based on the experimental schedule. The concentration profiles of the reaction products in the prolonged test run are presented in Fig. 6. Isoeugenol already reacts to form dihydroeugenol during the heating of the reactor to the reaction temperature of 300 °C. Upon reaching the target temperature and starting the mixing, the major compound in the reactor is dihydroeugenol. Other major compounds that increased sharply at the start of the reaction were the GC-undetectable compounds, as well as the diol product propyl catechol. The amount of GC-undetectable compounds and propyl catechol reached a plateau after 30 min of reaction, then started to decrease slowly. The most significant product of these compounds was propyl phenol, which increased steadily during the reaction time. Furthermore, the concentration of deoxygenated products, such as propyl benzene, propyl cyclohexene and propyl cyclohexane, increased steadily. Detected minor products include the dihydroeugenol dehydration product propyl anisole, and the methyl substitution product methyl propyl phenol. Bui and coworkers[57] presented a similar product distribution as a mixture of saturated and unsaturated cyclic

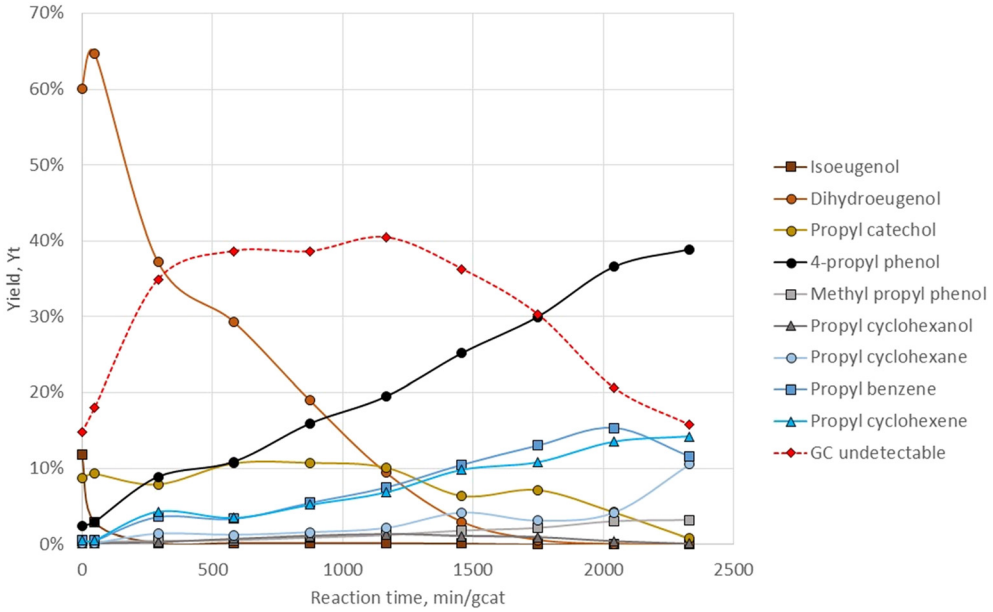

Fig. 6 Yields of the products as a function of reaction time in a prolonged test run with CatCen3.

hydrocarbons in guaiacol HDO, under similar conditions, over unsupported CoMoS catalysts.

The gas phase was analysed to monitor potential cracking products. No significant products other than methane, as a demethanation product from the methoxy group and the sulfiding agent DMDS, were detected in the gas phase. The results of gas phase analyses are presented in the SI.

Based on the HDO product distribution illustrated in Fig. 6, the reaction scheme presented in Scheme 1 is proposed. To evaluate the results, the products were divided into four groups: deoxygenated products (DO), consisting of non-oxygen-containing compounds; products containing one oxygen, such as propyl phenol (1-O); products with two oxygen atoms, mainly propyl catechol (2-O); and undetected

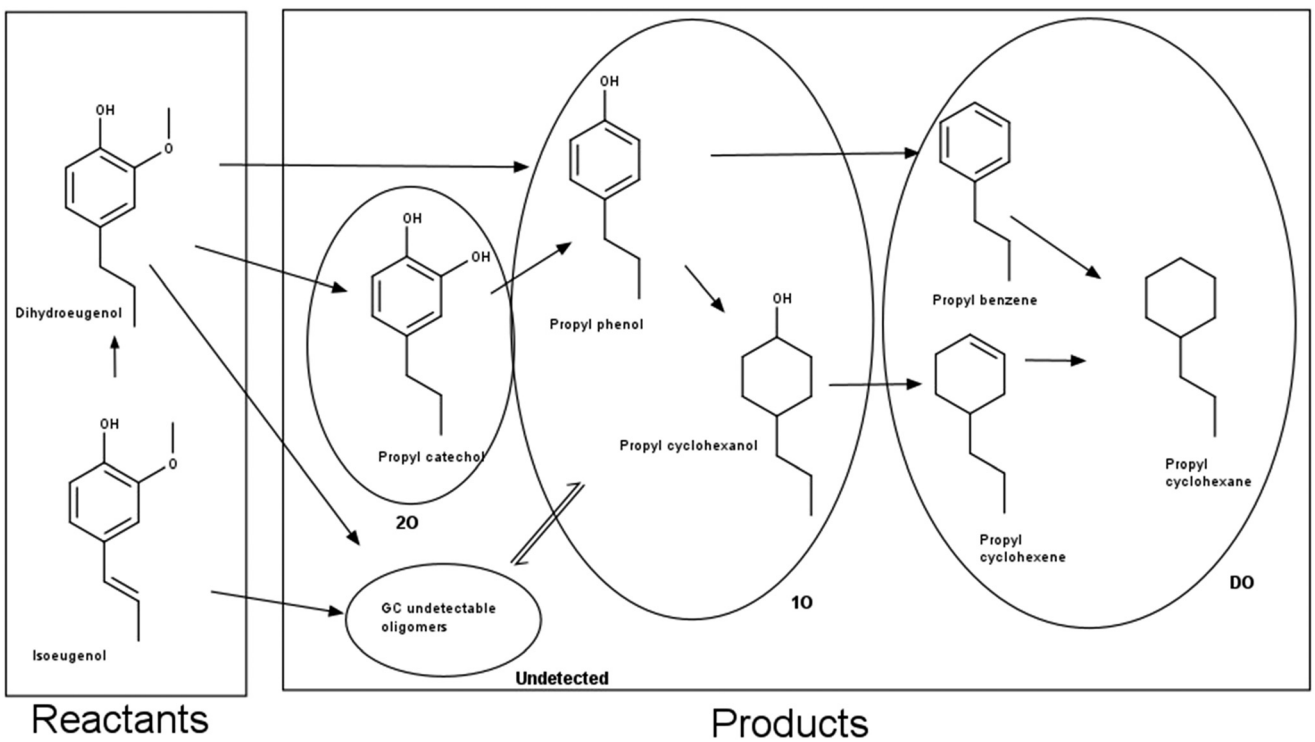

Scheme 1 Reaction scheme of isoeugenol hydrodeoxygenation, and the product groups: undetected, two oxygen-containing products (2O), one oxygen-containing products (1O), and deoxygenated products (DO).

products (undetected), defined as the difference between initial isoeugenol and detected products. These groups are visualized in Scheme 1. Significant differences in the product distribution are visible depending on the catalyst, as shown in Fig. I in the SI. Furthermore, the main compounds in a blank run without a catalyst were isoeugenol and dihydroeugenol, while conversions of 65–100% were reached with the catalysts, giving yields of the fully deoxygenated product of 5–24%.

4 Discussion

Based on the preparation, characterization, especially XRD data, and reaction performance, the prepared catalysts can be divided into two groups, *i.e.* sulfidic and oxidic catalysts (Cat-111, Cat-110, CatCen materials as sulfides, Cat-001, Cat-101 and Cat-100 as oxides). In addition to these two groups, two catalysts, Cat-000 and Cat-010, displayed an amorphous nature and exceptional reaction performance; these are discussed separately.

These catalyst groups are now discussed from the aspects of catalyst characterization to reaction performance, to conclude the optimal design and preparation method for bio-oil hydrotreatment catalyst.

4.1 Catalytic behavior

In the reaction tests, sulfide catalysts performed consistently better than oxides in terms of isoeugenol and dihydroeugenol conversion. As seen in Fig. 7, an average conversion of 70% was achieved with the sulfide catalysts at 750 min g_{cat}^{-1}, while the oxide catalysts required 1500 min g_{cat}^{-1} to reach a similar conversion level.

The difference in the reaction rate for the catalyst groups was clearly observed when the calculated reaction rates were grouped accordingly, as shown in Fig. 8.

Interestingly, when the mass balance of the liquid phase products LPMB is plotted as a function of conversion, the catalysts form two separate groups, as seen in Fig. 9. Catalytically less active oxide catalysts had, on average, roughly 10% better mass balance over the studied conversion range than other studied catalysts, including sulfides and Cat-000. The mass balance decrease was expected to be caused by the formation of non-GC-detectable compounds, such as oligomers. Potential reasons for the observed decreased mass balance can be identified as 1) sulfide-catalyzed oligomerization or 2) oligomerization of products produced with a more active catalyst.

Indeed, when the yields of the product groups were plotted as a function of conversion, as seen in Fig. 10, it was observed that the higher conversions with the sulfide catalysts arose mainly from higher yields of undetected compounds. The yields of 1-O compounds (mainly propyl phenol) and 2-O compounds (propyl catechol) were in the same region, as oxide catalysts yield 26% of 1-O and 13% of 2-O products at 80% conversion, compared to the sulfide catalyst with 19% and 11%, respectively. However, as the conversion increases, the amount of undetected compounds decreases quickly, as seen in both Fig. 9 and 10, highlighting the reversibility of the mass-balance loss and the intermediate role of the undetected compounds.

An obvious difference between sulfide and oxide catalysts was also the higher deoxygenation activity of the sulfide catalysts, as the yield of deoxygenated compounds follows the formation of partly deoxygenated 1-O compounds (black and blue curves in Fig. 10). It was concluded that the oxide catalysts favor the formation of 2-O and especially 1-O

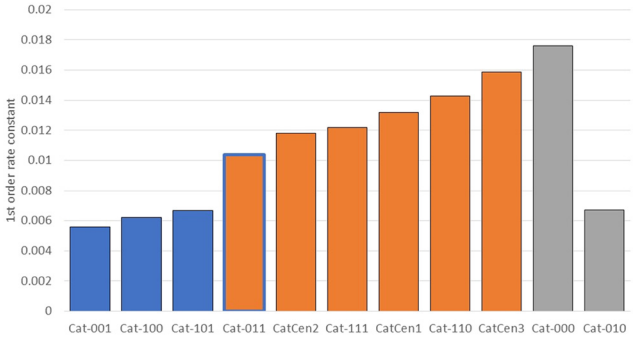

Fig. 8 Calculated rate constants for the tested catalysts. Blue: oxide, orange: sulfide, and grey: amorphous.

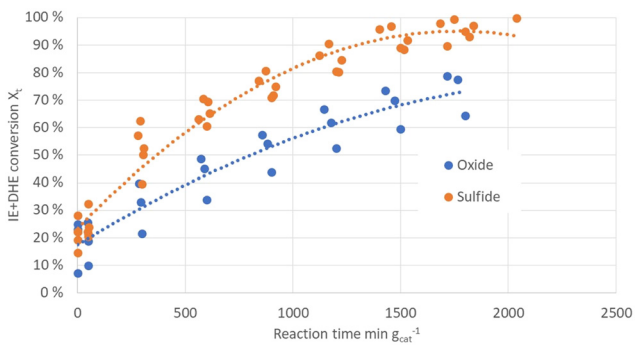

Fig. 7 Conversion as a function of reaction time with different catalyst groups. CatCen, Cat-111 and Cat-110 are classified as sulfides, and Cat-001, Cat-100 and Cat-101 are classified as oxides.

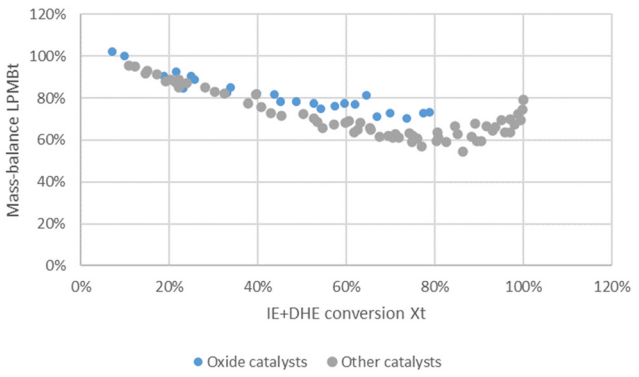

Fig. 9 Mass-balance as a function of observed conversion, including all test runs.

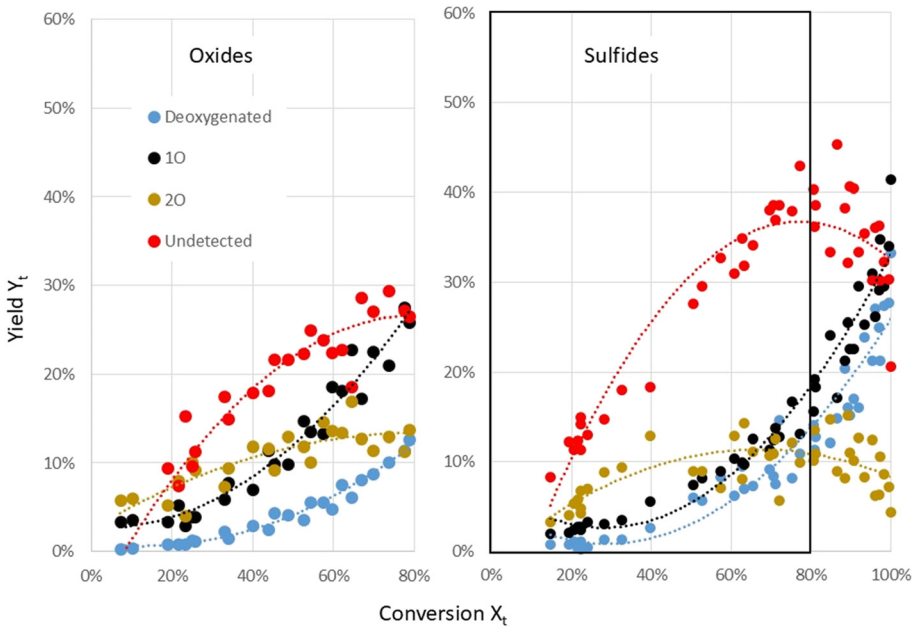

Fig. 10 The yield of compounds (deoxygenated (blue), 1-oxygen (black), 2-oxygen (yellow) and undetected (red)) as a function of conversion for oxide (left; catalysts Cat-001, Cat-101, and Cat-100) and sulfide (right; Cat-111, Cat-110, Cat-011, CatCen) catalysts. Conversions in the range from 0% to 80% are highlighted for sulfide in comparison to oxides.

compounds, while the sulfide catalysts generated undetected oligomers and efficiently converted 1-O compounds to deoxygenated compounds. The same is also observed from the selectivities calculated for the conversion range 30–80% in Fig. 11. As an interesting note on this observation, when comparing the activity of MoO_2 and different MoS_2 catalysts in the HDO of solvolyzed lignocellulosic biomass, Grilc *et al.*[58] reported no significant difference in performance with most studied catalysts.

In addition to the catalyst phase structure of the sulfide and oxide, the catalyst surface area also correlated with observed catalytic activity, as seen in Fig. 12 below. Catalyst Cat-000, with a high surface area, reached the highest conversion, and the center point catalysts, with higher surface areas, surpassed, on average, the other sulfide catalysts. Similarly, increased pore volume (correlating with surface area) was observed to increase the reaction rate and therefore conversion, as shown in Fig. 12 B. The higher activity of the higher surface area catalysts could be explained either by a higher number of active sites formed on the higher surface area or by better availability of the active sites in catalysts with a higher pore volume. Wang *et al.*[52] investigated the synthesis and hydrodeoxygenation properties of MoS_2 catalysts and observed a similar effect of pore volume, reporting that the pore volume was the main descriptor for catalyst activity in the HDO of *p*-cresol. The increase in the activity was assigned to the bimodal structure of the catalysts.[52] The oxide catalysts showed low conversion

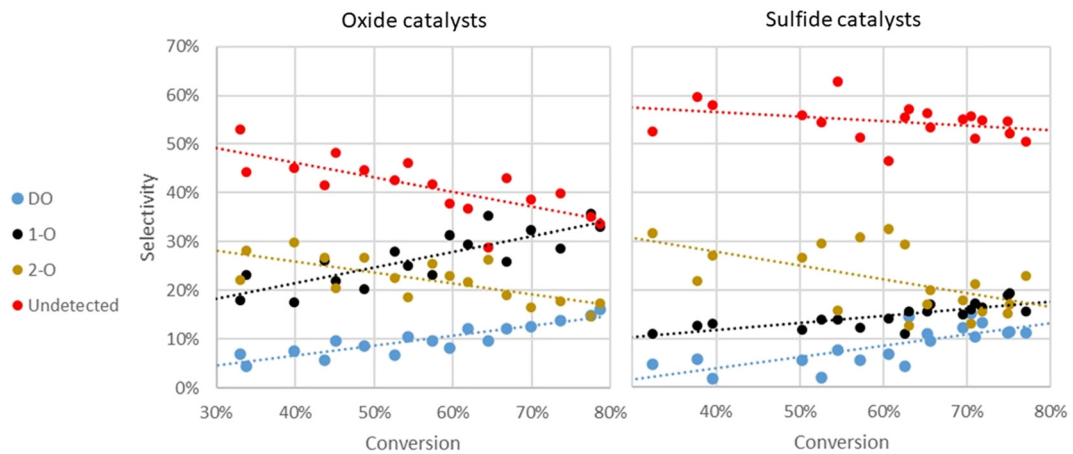

Fig. 11 Calculated selectivity for oxide and sulfide catalysts as a function of conversion; oxide catalysts (left) Cat-001, Cat-101, and Cat-100, and sulfide catalysts (right) Cat-111, Cat-110, Cat-011, and CatCen.

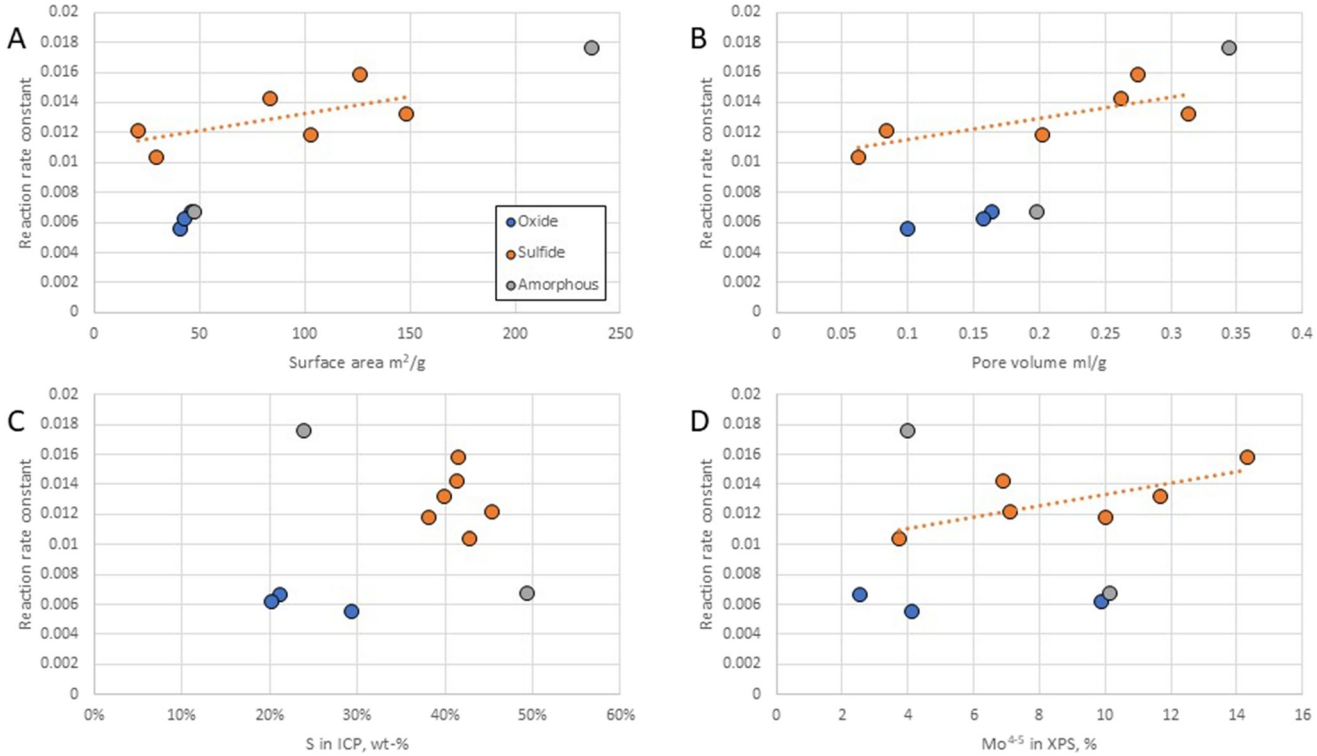

Fig. 12 The observed rate constants as a function of A) surface area; B) pore volume; C) sulfur content of the catalyst as determined by the ICP measurement; and D) mixed phase Mo (ref. 4 and 5) content of the catalyst as observed in the XPS. Oxides include the catalysts Cat-001, Cat-101, Cat-100, and sulfides include the Cat-111, Cat-110, Cat-011, CatCen catalysts.

regardless of the moderate surface area, highlighting the role of the chemical nature of the catalyst in activity, as shown in Fig. 12 C. Another good descriptor for conversion is the sulfur defects identified as mixed phase Mo^{4-5+} in the XPS of the CatCen and sulfide catalysts, as presented in Fig. 12 D. This mixed phase was assigned to mixed sulfide phases or, especially, Co–Mo–S, which is known to be an active phase in HDO.[25]

When comparing the selectivity to deoxygenated products at the reference conversion level of 50%, higher selectivity was reached with catalysts with higher activity, *i.e.* high rate constant, as seen in Fig. 13A. Among the sulfide catalysts, overall sulfur content, and especially high sulfide content, as measured by XPS, and a high amount of cobalt in sulfide form (CoS_2) were observed to correlate with higher deoxygenation selectivity, as presented in Fig. 13. A low sulfide and cobalt sulfide content also explains the poor deoxygenation activity of the Cat-000 catalyst, which high reaction rate constant would otherwise predict high deoxygenation activity, highlighted in Fig. 13A.

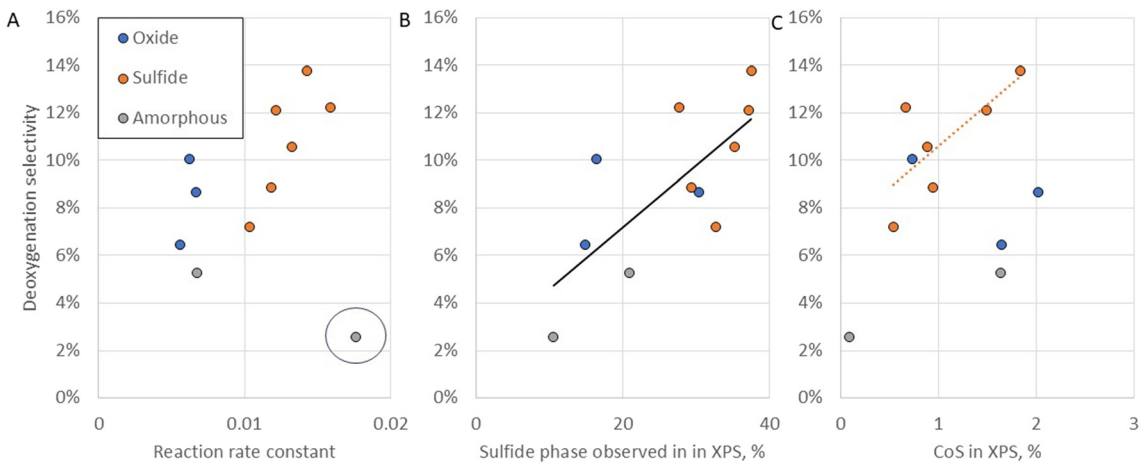

Fig. 13 Deoxygenation selectivity at 50% conversion as a function of A) calculated reaction rate constant, B) sulfide content in XPS, and C) CoS_2 content in XPS.

Two outliers of the reaction tests were Cat-000 and Cat-010 catalysts, which displayed low crystallinity according to XRD characterization. Cat-000 stood out with the highest conversion and 1-O selectivity compared to oxide catalysts, essentially propyl phenol. At a high conversion of 90%, 42% selectivity to propyl phenol and other 1-O compounds was observed (Fig. 14). However, lower selectivity to deoxygenated products was detected, which was assigned to the oxidic nature and low cobalt content. The formation of undetected oligomers was also on the same level as observed for the sulfide catalysts. One explanation for the high activity of the demethoxylation could be the highest proportion of Mo^{5+} surface atoms, which were considered responsible for the high deoxygenation activity by Zhou and co-workers.[48] Other obvious reasoning is the high surface area of 242 m^2 g^{-1}, which could increase the number and availability of active sites.

The Cat-010 catalyst displayed a low overall conversion and deoxygenation activity. The most abundant products were undetected compounds, as well as propyl catechol. The selectivity to 1-O compounds was at the same level as observed for sulfide catalysts, but no increase in the formation of deoxygenated compounds was detected. One potential explanation can be linked to the XPS results, which indicated exceptionally high content of sulfur in Cat-010, connected to the peak at 163.3 eV, which was interpreted as partially oxidized sulfides.

From the reaction results, three trends can be highlighted. First, the catalysts with a highly sulfidic nature displayed significantly higher conversion under the studied conditions than the catalysts with higher oxygen content. However, high activity resulted in mainly undetected compounds, which were converted to at least partially deoxygenated products as the reaction proceeded. Second, the conversion of isoeugenol and dihydroeugenol was strongly affected by the surface area and pore volume, probably affecting the amount and availability of the active sites, as well as the speciation of molybdenum in the catalyst, as shown in Fig. 12. Third, the deoxygenation activity of the catalyst was highly dependent on the amount of molybdenum and cobalt sulfides on the catalyst surface, as seen in Fig. 13.

In addition, the high-activity sulfidic catalysts prepared in this study achieve the same or higher performance in terms of conversion of oxygenates as both supported sulfided catalysts and unsupported catalysts reported in the literature for similar model compounds. A comparison of the best catalyst presented in this study and the results obtained with 1-O and 2-O containing model compounds presented in the literature is presented in Fig. 15; the data are listed in tabulated form in the SI.

4.2 Effect of catalyst preparation parameters

In subchapter 4.1, the behavior of the catalysts in the experiments was related to the properties of the prepared catalytic materials based on the characterization results. In this subchapter, the relationship between the preparation conditions and material properties is discussed for the design of a hydrotreatment catalyst with high activity and selectivity to deoxygenated products.

Grouping of the catalysts also reflects the variation in the parameters of catalyst preparation. Amorphous catalysts Cat-000 and Cat-010 were synthesized at a low T of 200 °C and a low pH of 0. Otherwise, a low sulfur amount results in oxide materials, while a more than stoichiometric amount of sulfur leads to the formation of

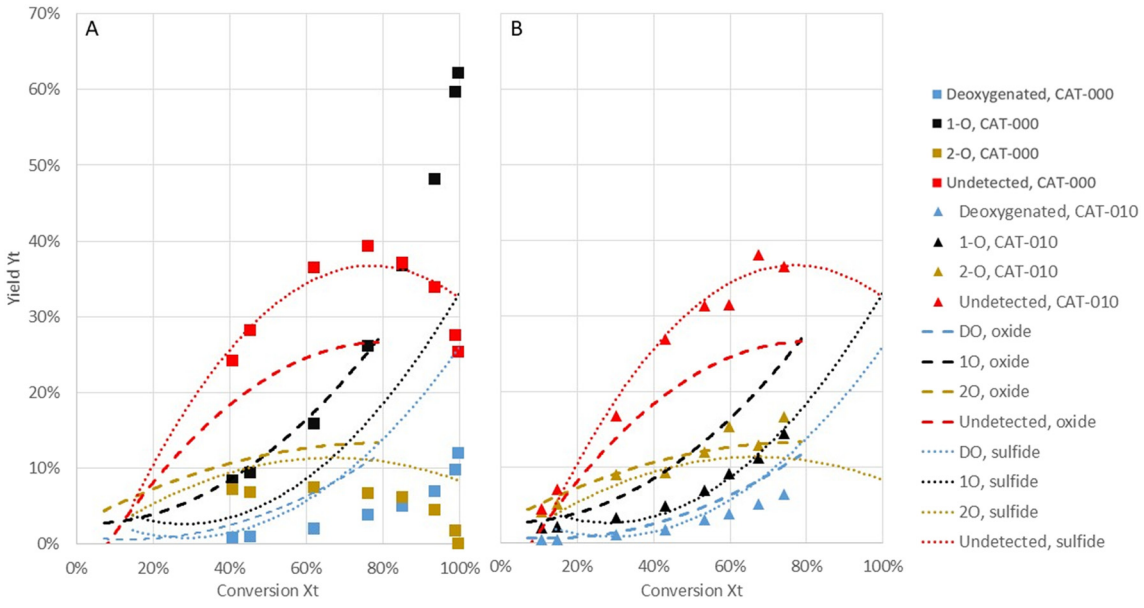

Fig. 14 The yield of products as a function of conversion with Cat-000 (A) and Cat-000 (B) catalysts as markers. Dotted lines represent fitted curves for oxide and sulfide catalysts from Fig. 10.

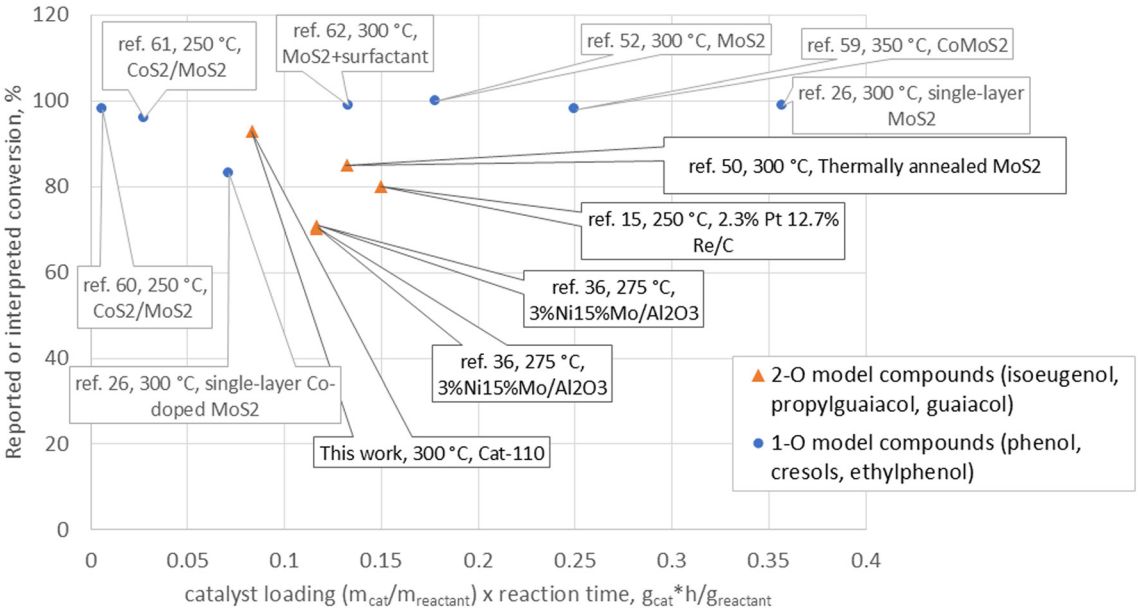

Fig. 15 Catalyst performance comparison visualization with results presented in the literature, normalized with respect to catalyst-to-reactant ratio and reaction time.[15,26,36,50,52,59–62]

sulfides. It is assumed that the low sulfur amount of S/(Mo × 2) = 1 was not adequate for the formation of active sulfide phases in the case of oxide catalysts Cat-001, Cat-101 and Cat-100, and the low temperature used in the synthesis of Cat-001 also hindered the formation of MoO_2.

The center point CatCen catalysts are also considered sulfides based on the characterization data, which proposes the minimum sulfur amount for catalyst synthesis to be 1.5 times higher than the stoichiometric amount. A high temperature of a minimum of 220 °C increased the formation of sulfides, as the Cat-011 catalyst consists of a mixture of sulfide and oxide, even performing similarly to sulfides. The dependency of the catalyst type on the preparation conditions is presented in Fig. 16.

To summarize, for optimal conversion, high surface area and pore volume of the catalyst were observed to correlate with good catalytic performance. From the studied catalyst preparation parameters, the combination of high sulfur content and especially low pH has the most significant effect on the surface area and therefore also on the achieved conversion, as seen in Fig. 17. Consistent with this, Wang *et al.*[52] also observed that low pH increased the pore volume for the preparation of MoS_2 *via* the hydrothermal method.

On the other hand, to achieve high selectivity for deoxygenated products, a high sulfur content was desired. From the preparation parameters, both a high S content and a high synthesis temperature increased the selectivity to deoxygenated products, as seen in Fig. 18. The increase was assigned to increased formation of sulfides, and especially cobalt sulfide CoS_2, during preparation of catalysts at high temperatures of 220 and 240 °C, as presented in Fig. 18B and C. The role of increased sulfides in deoxygenation selectivity was discussed previously (Fig. 13).

To conclude, for an optimal HDO catalyst with high selectivity to deoxygenated products and high conversion, a high catalyst synthesis temperature can be recommended to increase deoxygenation selectivity. However, the selection of pH and the sulfur amount is challenging. pH had a significant effect on the surface area and, consequently, conversion; however, the optimum pH was 0.4 for the center point catalysts. Regarding sulfur loading, a higher loading increased the selectivity to deoxygenated products, but decreased the surface area and consequently conversion. Therefore, balancing the sulfur loading of the synthesis to the desired application was deemed to be the most crucial

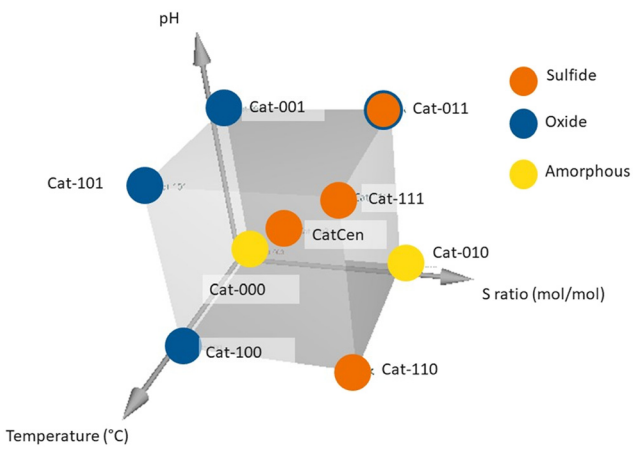

Fig. 16 Catalyst grouping in the design space.

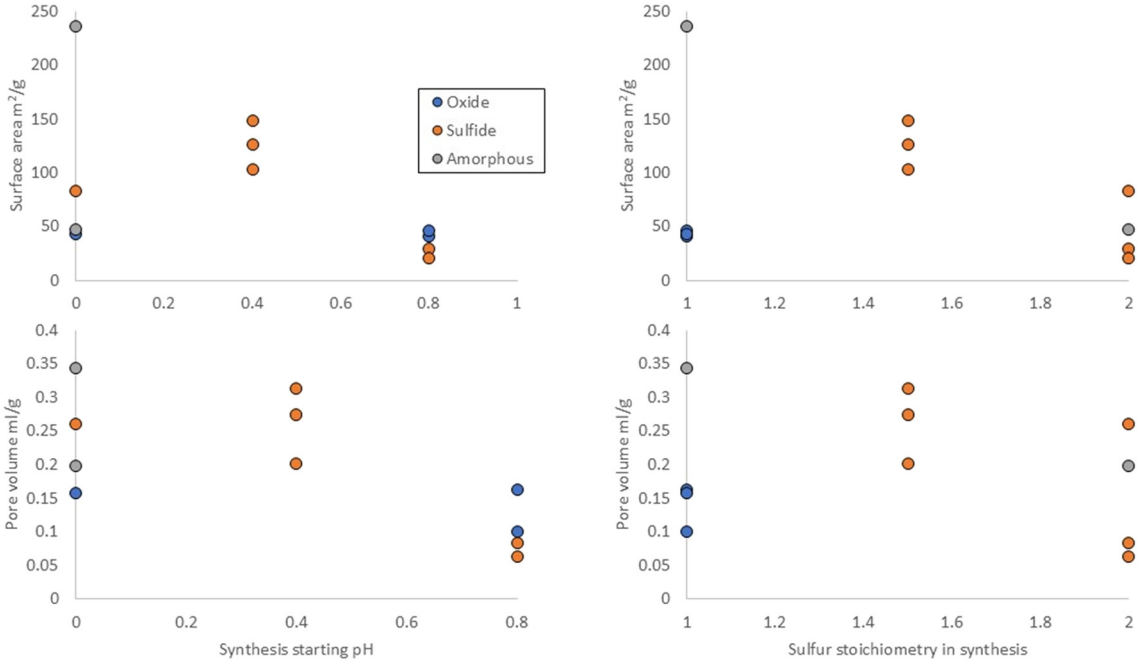

Fig. 17 Effect of the pH and sulfur excess preparation parameters on the surface area and pore volume of the prepared catalysts.

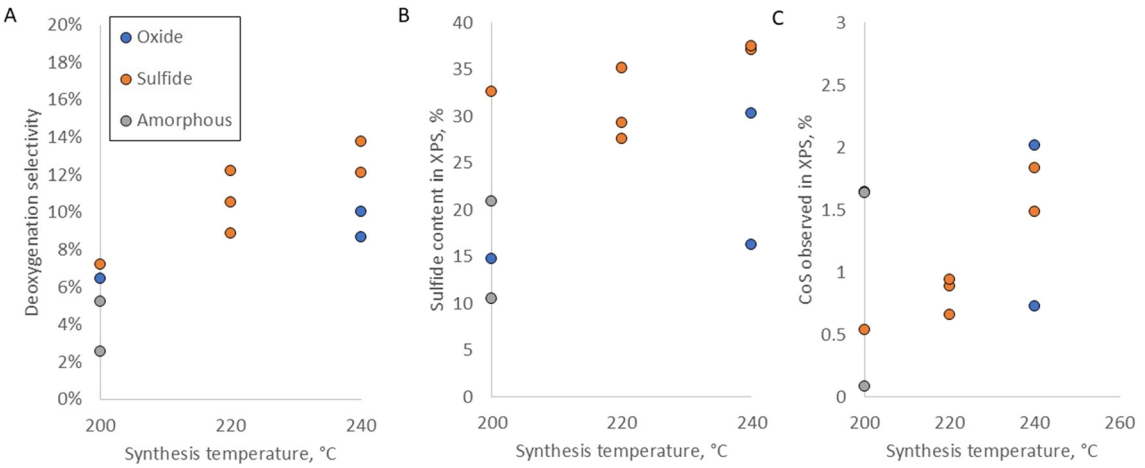

Fig. 18 Effect of the preparation temperature on the selectivity to deoxygenated products.

parameter in the synthesis of catalysts for the hydrodeoxygenation reactions.

5 Conclusions

Eleven unsupported $CoS_2MoS_xO_{2-x}$ catalysts were synthesized by hydrothermal precipitation, giving mixtures of mainly CoS_2, MoS_2 and MoO_x, depending on the studied preparation parameters (temperature, the ratio between sulfur and Mo, and pH). The prepared catalysts were characterized and tested for the HDO of the bio-oil model compound isoeugenol.

The amount of sulfur in the catalyst synthesis was found to be critical for the formation of the active sulfide phase. The catalysts synthesized with a low amount of sulfur were found to be mixtures of Mo oxide phases and CoS_2. Three of the four catalysts prepared with a low sulfur loading were characterized to have a low surface area of 40–50 $m^2\ g^{-1}$ and poor activity in the HDO of isoeugenol. These Mo-oxide catalysts successfully facilitated the hydrogenation of the double bond of isoeugenol and the demethylation or demethoxylation of the methoxy group to the hydroxyl group to form propyl catechol and propyl phenol as major products.

One particular catalyst with low sulfur amount, prepared at low T and low pH, was characterized as mainly oxide material with an extremely high surface area of 236 $m^2\ g^{-1}$ and a high activity for the demethoxylation of isoeugenol,

reaching full conversion and considerably high selectivity to phenolic products containing one oxygen atom, 62%, mainly propyl phenol. The high activity and selectivity were ascribed to the high surface area and high pore volume, which increased the amount and availability of active sites, as the product distribution was similar to that of other oxide catalysts with smaller surface areas.

With a high sulfur content of 1.5 and 2 times the stoichiometric amount during catalyst synthesis, sulfides were formed as mixtures of MoS_2, MoO_2 and CoS_2 crystalline phases. Among these catalysts, the surface area was found to be the most significant parameter affecting the conversion of isoeugenol and dihydroeugenol. These catalysts, with a higher sulfur content, afforded higher selectivity for deoxygenated products. The main products in the screening experiments with catalysts with mainly sulfide phases were propyl phenol, propyl cyclohexene, propyl benzene and propyl cyclohexane. A deoxygenated product yield of 28% was reached with the most active deoxygenation catalyst.

In the reaction experiments, the reversible formation of GC undetectable byproducts as the reaction progressed decreased the mass balance closure. Increased formation of the undetected oligomers was observed with more active catalysts. A careful selection of the model compound is recommended for future work, as multiple investigators have reported excellent mass-balance closures with similar compounds, most importantly dihydroeugenol.[19,50]

For the synthesis of an optimal HDO catalyst in the design space, low to medium pH is recommended for increasing the surface area, a high synthesis temperature of 240 °C for elevated selectivity for deoxygenated products, while a sulfur excess of at least 1.5 forms the sulfide phase that is active in deoxygenation. Formation of CoS_2 was observed to increase the deoxygenation selectivity. A significant decrease in activity was detected for the oxide phases compared to the sulfide one, especially in the formation of deoxygenation products. This needs to be taken into account in the process design of HDO, as replacement of sulfur with oxygen deactivates the catalyst fast, and subsequent conditions that preserve the sulfide form of the catalyst are required. The performance of the most active HDO catalysts prepared in this investigation was observed to be superior to that of catalysts presented in the literature for similar model compound reactions.

Author contributions

Tyko Viertiö: conceptualization, data curation, formal analysis, investigation, methodology, visualization, writing – original draft; Niko Vuorio: investigation, methodology; Sari Rautiainen: methodology, writing – review & editing; Johanna Kihlman: conceptualization, writing – original draft; Matti Reinikainen: methodology, conceptualization; Alexander Reznichenko: conceptualization, funding acquisition, project administration, supervision, writing – review & editing; Kristoffer Meinander: investigation, writing – review & editing; Dmitry Yu. Murzin: conceptualization, writing – review & editing; and Juha Lehtonen: conceptualization, writing – review & editing.

Conflicts of interest

There are no conflicts to declare.

Data availability

The data supporting this article have been included as part of the supplementary information (SI).

Supplementary information: SI contains additional characterization and reaction test results, including ICP, SEM, physisorption and XPS results, as well as gas phase data from reaction experiments and fitting of the rate constants. See DOI: https://doi.org/10.1039/d4cy01503g.

Acknowledgements

This work was supported by Business Finland within the CaSH research project, grant 43385/31/202. Yukho Sok-Sar is acknowledged for technical assistance in catalyst preparation. Tiina Heikola, from VTT Technical Research Center of Finland, and Mikko Heikkilä, from the University of Helsinki, are acknowledged for carrying out the ICP and XRD analyses, respectively. Matti Reinikainen and Emil Högnabba are acknowledged for preliminary experiments and method development.

References

1 IEA, *Renewable Energy Market Update - June 2023*, Paris, 2023.
2 IEA, *Renewables 2022*, Paris, 2022.
3 IEA, Task 39: Biofuels to decarbonize transport: Definitions, https://task39.ieabioenergy.com/about/definitions/.
4 S. Khalili, E. Rantanen, D. Bogdanov and C. Breyer, *Energies*, 2019, **12**, 3870.
5 D. Chiaramonti, G. Talluri, N. Scarlat and M. Prussi, *Renewable Sustainable Energy Rev.*, 2021, **139**, 110715.
6 IEA, *Net Zero by 2050*, Paris, 2021.
7 E. U. A. S. Agency, *EUROPEAN AVIATION ENVIRONMENTAL REPORT 2022*, 2022.
8 D. C. Elliott, H. Wang, R. French, S. Deutch and K. Iisa, *Energy Fuels*, 2014, **28**, 5909–5917.
9 E. Pienihäkkinen, C. Lindfors, T. Ohra-aho and A. Oasmaa, *Energy Fuels*, 2022, **36**, 3654–3664.
10 A. Oasmaa, J. Lehto, Y. Solantausta and S. Kallio, *Energy Fuels*, 2021, **35**, 5683–5695.
11 A. P. Pinheiro Pires, J. Arauzo, I. Fonts, M. E. Domine, A. Fernández Arroyo, M. E. Garcia-Perez, J. Montoya, F. Chejne, P. Pfromm and M. Garcia-Perez, *Energy Fuels*, 2019, **33**, 4683–4720.
12 S. Wijeyekoon, K. Torr, H. Corkran and P. Bennett, *Commercial status of direct thermochemical liquefaction technologies technologies*, 2020.
13 A. H. Zacher, D. C. Elliott, M. V. Olarte, H. Wang, S. B. Jones and P. A. Meyer, *Biomass Bioenergy*, 2019, **125**, 151–168.
14 E. Furimsky, *Appl. Catal., A*, 2000, **199**, 147–190.

15 M. Martinez-Klimov, P. Mäki-Arvela, A. Çiftçi, N. Kumar, K. Eränen, M. Peurla, E. J. M. Hensen and D. Y. Murzin, *ACS Eng. Au*, 2022, **2**, 436–449.
16 A. R. Ardiyanti, A. Gutierrez, M. L. Honkela, A. O. I. Krause and H. J. Heeres, *Appl. Catal., A*, 2011, **407**, 56–66.
17 Z. Vajglová, B. Gauli, P. Mäki-Arvela, N. Kumar, K. Eränen, J. Wärnå, R. Lassfolk, I. L. Simakova, I. P. Prosvirin, M. Peurla, J. K. M. Lindén, H. Huhtinen, P. Paturi, D. E. Doronkin and D. Y. Murzin, *ACS Appl. Nano Mater.*, 2023, **6**, 10064–10077.
18 Z. Vajglová, B. Gauli, P. Mäki-Arvela, I. L. Simakova, N. Kumar, K. Eränen, T. Tirri, R. Lassfolk, M. Peurla, D. E. Doronkin and D. Y. Murzin, *J. Catal.*, 2023, **421**, 101–116.
19 Z. Vajglová, O. Yevdokimova, A. Medina, K. Eränen, T. Tirri, J. Hemming, J. Lindén, I. Angervo, P. Damlin, D. E. Doronkin, P. Mäki-Arvela and D. Y. Murzin, *Sustainable Energy Fuels*, 2023, **7**, 4486–4504.
20 W. Yin, Z. Wang, H. Yang, R. H. Venderbosch and H. J. Heeres, *Energy Fuels*, 2022, **36**, 14281–14291.
21 S. Boullosa-Eiras, R. Lødeng, H. Bergem, M. Stöcker, L. Hannevold and E. A. Blekkan, *Catal. Today*, 2014, **223**, 44–53.
22 D. C. Elliott, *Energy Fuels*, 2007, **21**, 1792–1815.
23 M. V. Olarte, A. H. Zacher, A. B. Padmaperuma, S. D. Burton, H. M. Job, T. L. Lemmon, M. S. Swita, L. J. Rotness, G. N. Neuenschwander, J. G. Frye and D. C. Elliott, *Top. Catal.*, 2016, **59**, 55–64.
24 E. Furimsky, *Catal. Today*, 2013, **217**, 13–56.
25 J. Cao, Y. Zhang, X. Liu, C. Zhang and Z. Li, *Fuel*, 2023, **334**, 126640.
26 G. Liu, A. W. Robertson, M. M.-J. Li, W. C. H. Kuo, M. T. Darby, M. H. Muhieddine, Y.-C. Lin, K. Suenaga, M. Stamatakis, J. H. Warner and S. C. E. Tsang, *Nat. Chem.*, 2017, **9**, 810–816.
27 A. Duval and M. Lawoko, *React. Funct. Polym.*, 2014, **85**, 78–96.
28 X. Chen, K. A. Orton, C. Mukarakate, K. Gaston, G. M. Fioroni, R. L. McCormick, M. B. Griffin and K. Iisa, *Sustainable Energy Fuels*, 2024, **8**, 5504–5513.
29 M. Alda-Onggar, P. Mäki-Arvela, K. Eränen, A. Aho, J. Hemming, P. Paturi, M. Peurla, M. Lindblad, I. L. Simakova and D. Y. Murzin, *ACS Sustainable Chem. Eng.*, 2018, **6**, 16205–16218.
30 L. Bomont, M. Alda-Onggar, V. Fedorov, A. Aho, J. Peltonen, K. Eränen, M. Peurla, N. Kumar, J. Wärnå, V. Russo, P. Mäki-Arvela, H. Grénman, M. Lindblad and D. Y. Murzin, *Eur. J. Inorg. Chem.*, 2018, **2018**, 2841–2854.
31 C. Lindfors, P. Mäki-Arvela, P. Paturi, A. Aho, K. Eränen, J. Hemming, M. Peurla, D. Kubička, I. L. Simakova and D. Y. Murzin, *ACS Sustainable Chem. Eng.*, 2019, **7**, 14545–14560.
32 M. E. Martínez-Klimov, P. Mäki-Arvela, Z. Vajglová, C. Schmidt, O. Yevdokimova, M. Peurla, N. Kumar, K. Eränen and D. Y. Murzin, *Top. Catal.*, 2023, **66**, 1296–1309.
33 M. E. Martínez-Klimov, O. Yevdokimova, P. Mäki-Arvela, J. Cueto, N. Shcherban, Z. Vajglová, K. Eränen and D. Y. Murzin, *Sustainable Energy Fuels*, 2024, **8**, 90–102.
34 A. Bjelić, M. Grilc and B. Likozar, *Chem. Eng. J.*, 2018, **333**, 240–259.
35 A. Bjelić, M. Grilc, M. Huš and B. Likozar, *Chem. Eng. J.*, 2019, **359**, 305–320.
36 T. Ročnik Kozmelj, M. Žula, J. Teržan, B. Likozar, U. Maver, L. Činč Ćurić, E. Jasiukaitytė-Grojzdek and M. Grilc, *J. Cleaner Prod.*, 2023, **414**, 137701.
37 G. Bellussi, G. Rispoli, A. Landoni, R. Millini, D. Molinari, E. Montanari, D. Moscotti and P. Pollesel, *J. Catal.*, 2013, **308**, 189–200.
38 N. Bergvall, L. Sandström, F. Weiland and O. G. W. Öhrman, *Energy Fuels*, 2020, **34**, 8452–8465.
39 N. Bergvall, R. Molinder, A.-C. Johansson and L. Sandström, *Energy Fuels*, 2021, **35**, 2303–2312.
40 A. Dimitriadis, N. Bergvall, A. C. Johansson, L. Sandström, S. Bezergianni, N. Tourlakidis, L. Meca, P. Kukula and L. Raymakers, *Fuel*, 2023, **332**, 126153–126153.
41 N. Bergvall, Y. W. Cheah, C. Bernlind, A. Bernlind, L. Olsson, D. Creaser, L. Sandström and O. G. W. Öhrman, *Fuel Process. Technol.*, 2024, **253**, 108009.
42 J. Cao, Y. Zhang, L. Wang, C. Zhang and C. Zhou, *Front. Chem.*, 2022, **10**, 928806.
43 K. Wu, W. Wang, H. Guo, Y. Yang, Y. Huang, W. Li and C. Li, *ACS Energy Lett.*, 2020, **5**, 1330–1336.
44 K. Wu, X. Li, W. Wang, Y. Huang, Q. Jiang, W. Li, Y. Chen, Y. Yang and C. Li, *ACS Catal.*, 2022, **12**, 8–17.
45 J. Cao, A. Li, Y. Zhang, L. Mu, X. Huang, Y. Li, T. Yang, C. Zhang and C. Zhou, *Mol. Catal.*, 2021, **505**, 111507.
46 C. Zhang, K. Liu, Y. Zhang, L. Mu, Z. Zhang, J. Huang, Y. Wang, T. Yang, J. Cao and C. Zhou, *Appl. Catal., A*, 2021, **621**, 118175.
47 J. Cao, A. Li, Y. Zhang, L. Mu, X. Huang, Y. Li, T. Yang, C. Zhang and C. Zhou, *Mol. Catal.*, 2021, **505**, 1–9.
48 W. Zhou, T. Zhang and F. Yang, *Ind. Eng. Chem. Res.*, 2023, **62**, 10409–10418.
49 Y. Zhang, T. Liu, Q. Xia, H. Jia, X. Hong and G. Liu, *J. Phys. Chem. Lett.*, 2021, **12**, 5668–5674.
50 Y. W. Cheah, M. A. Salam, J. Sebastian, S. Ghosh, O. Öhrman, D. Creaser and L. Olsson, *Sustainable Energy Fuels*, 2021, **5**, 5270–5286.
51 T. Viertiö, J. Lehtonen, J. Kihlman, L. Sokka, A. Reznichenko, V. Tuppurainen, S. Ala-Kokko, S. Seppä, J. Tanskanen, J. Ahola, D. Murzin, Z. Vajglova, P. Mäki-Arvela and N. Kumar, *CaSH - Catalytic Slurry Hydrotreatment*, VTT Technical Research Centre of Finland, 2024.
52 W. Wang, L. Li, K. Wu, G. Zhu, S. Tan, W. Li and Y. Yang, *RSC Adv.*, 2015, **5**, 61799–61807.
53 M. Thommes, K. Kaneko, A. V. Neimark, J. P. Olivier, F. Rodriguez-Reinoso, J. Rouquerol and K. S. W. Sing, *Pure Appl. Chem.*, 2015, **87**, 1051–1069.
54 N. Joseph, J. S. Sethulakshmi and A. C. Bose, *J. Mater. Sci.: Mater. Electron.*, 2020, **31**, 12684–12695.
55 J. Joseph, M. J. Rasmussen, J. P. Fecteau, S. Kim, H. Lee, K. A. Tracy, B. L. Jensen, B. G. Frederick and E. A. Stemmler, *Energy Fuels*, 2016, **30**, 4825–4840.
56 T. Nakamura, H. Kawamoto and S. Saka, *J. Wood Chem. Technol.*, 2007, **27**, 121–133.
57 V. N. Bui, D. Laurenti, P. Delichère and C. Geantet, *Appl. Catal., B*, 2011, **101**, 246–255.
58 M. Grilc, G. Veryasov, B. Likozar, A. Jesih and J. Levec, *Appl. Catal., B*, 2015, **163**, 467–477.

59 B. Yoosuk, D. Tumnantong and P. Prasassarakich, *Chem. Eng. Sci.*, 2012, **79**, 1–7.
60 W. Wang, L. Li, K. Wu, G. Zhu, S. Tan, Y. Liu and Y. Yang, *RSC Adv.*, 2016, **6**, 31265–31271.
61 W. Wang, K. Wu, S. Tan and Y. Yang, *ACS Sustainable Chem. Eng.*, 2017, **5**, 8602–8609.
62 W. Wang, K. Zhang, Z. Qiao, L. Li, P. Liu and Y. Yang, *Ind. Eng. Chem. Res.*, 2014, **53**, 10301–10309.